Bi_2O_3 Nanoflakes: A Cost Effective Drug

Luke D. Geoffrion[1], David Medina-Cruz[2], Matthew Kusper[1], Prakash Parajuli[3], Arturo Ponce[3], Thang Ba Hoang[4], Todd Brintlinger[5], Thomas J. Webster[2], Grégory Guisbiers[1,*]

[1]Department of Physics & Astronomy, University of Arkansas Little Rock, 2801 South University Avenue, Little Rock, AR 72204, USA

[2] Department of Chemical Engineering, Northeastern University, 313 Snell Engineering Center, 360 Huntington Avenue, Boston, MA 02115, USA

[3]Department of Physics & Astronomy, The University of Texas at San Antonio, One UTSA circle, San Antonio, TX 78249, USA

[4]Department of Physics & Materials Science, The University of Memphis, Memphis, TN 38152, USA

[5]U.S. Naval Research Laboratory, Nanoscale Materials Section, 4555 Overlook Ave SW, Washington, DC 20375, USA

*Corresponding author: gxguisbiers@ualr.edu

ORCID: Luke D. Geoffrion: https://orcid.org/0000-0003-4668-7453

ORCID: David Medina-Cruz: https://orcid.org/0000-0002-7658-583X

ORCID: Matthew Kusper: https://orcid.org/0000-0002-9239-6262

ORCID : Prakash Parajuli: http://orcid.org/0000-0001-6732-2010

ORCID : Arturo Ponce: http://orcid.org/0000-0001-5529-6468

ORCID: Thang Ba Hoang:

ORCID: Todd Brintlinger: http://orcid.org/0000-0001-7959-4769

ORCID: Thomas J. Webster: http://orcid.org/0000-0002-2028-5969

ORCID: Grégory Guisbiers: http://orcid.org/0000-0002-4615-6014

Abstract

Bismuth oxide is an important bismuth compound having applications in electronics, catalysis and medicine. At the nanoscale, bismuth oxide experiences a variety of new physico-chemical properties because of its increased surface to volume ratio leading potentially to new applications. In this manuscript, we report for the very first time the synthesis of bismuth oxide (Bi_2O_3) nano-flakes by pulsed laser ablation in liquids without any external assistance (no acoustic, electric field, or magnetic field). The synthesis was performed by irradiating, pure bismuth needles immerged into de-ionized water, at very high fluence ~159 J/cm^2 in order to be highly selective and only promote the growth of two-dimensional structures. The x- and y- dimensions of the flakes could reach microns in size while their thickness was kept around 50 nm. Finally, α- and γ-Bi_2O_3 nano-flakes were successfully synthesized displaying the following energy bandgap 2.53±0.01 eV and 1.88±0.01 eV, respectively. By using this mixture of flakes, we demonstrated that the nanostructures can be used as antimicrobial agents, achieving a complete inhibition of Gram positive (MSRA) and gram negative bacteria (MDR *E. coli*) at low concentration, ~50 ppm, while remaining cytocompatible at the same range of concentrations in human dermal fibroblasts assays. Besides, we tested the nanomaterials as anticancer agents with melanoma cells, showing a dose-dependent inhibition of cancer development over 3 days

Table of Contents Image

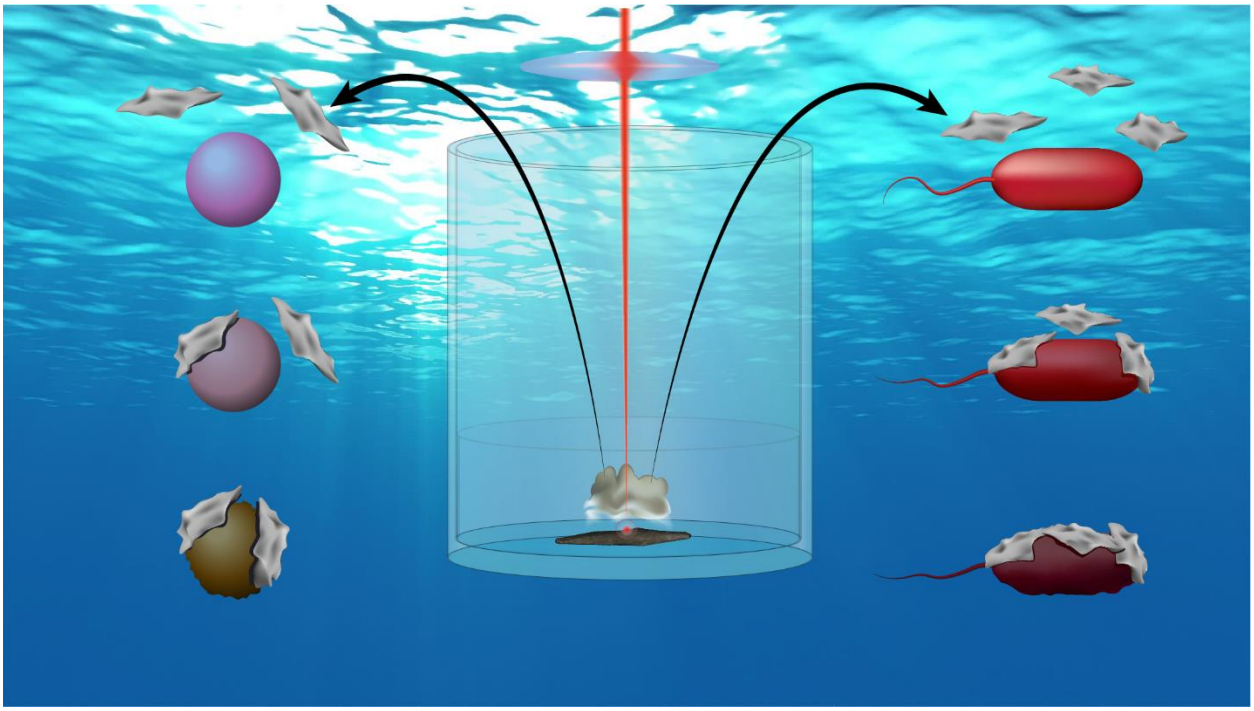

Bismuth oxide nano-flakes attacking gram positive and gram negative bacteria.

1. Introduction

When penicillin was discovered in September 1928 by Sir Alex Fleming, it changed the face of medicine [1, 2]. This “miracle drug,”, as it was known, was able to offer a cure for some of the most nefarious of diseases. It was only in 1942 that penicillin could be produced at an industrial scale and started to really make an impact in people’s daily life [1]. However, the dark side of the story is that due to the benefits of this new drug, doctors started prescribing it massively for all sorts of diseases and people even started to self-medicate themselves. But when antibiotics are overused or used inappropriately (i.e., when a patient does not finish a full course of treatment,), it helps hasten the spread of resistant bacteria. After a course of antibiotics, some naturally resistant bacteria will be left behind, survival-of-the-fittest style; the more frequently antibiotics are used, the more prevalent these fiercer strains will become. According to the World Health Organization, the inappropriate use of antibiotics in animal husbandry is an underlying contributor to the emergence and spreading of antibiotic-resistant germs, and consequently the use of antibiotics as growth promoters in animal feeds should be restricted [3]. Adjacent bacteria can also acquire resistance by mutating or exchanging genetic material with the resistant strains. When those treatment-resistant bacteria grow and multiply, they can lead to new infections that then become difficult or even impossible to treat. It has been estimated that by 2050, antibiotic-resistant bugs could kill an estimated 10 million people each year. Bacterial infections arise almost everywhere from drinking water [4, 5] to medical implants [6]. A way to address this problem is to look for new antibacterial nano-compounds by taking advantage of their physico-bio-chemical properties at the nanoscale.

Due to their wide variety of compositions, shapes and sizes, nanomaterials can be used as nanodelivery vehicles to target cancer cells as well as a sole therapeutics, using the intrinsic characteristics of some nanoparticles to trigger anticancer responses related to hyperthermia or radiotherapy [7, 8]. Especially metal nanoparticles have gained significant attention because of their unique physical and chemical. One of the most relevant features is their larger surface area and area: volume ratio, reason why metal NPs exhibit several specific physicochemical properties that make them useful for the treatment of cancer [7]. Metal nanoparticles have advantages over other nanoparticles because of their inherent anticancer activity, which often removed the need of the use of carriers for the delivery of therapeutic and diagnostic agents. Furthermore, they are biocompatible in nature and can be easily excreted from the body [9].

Indeed, at the nanoscale, quantum effects and a huge surface to volume ratio are responsible for the new physico-bio-chemical properties of materials [10, 11]. Various materials as noble metals [12, 13], transition elements [14], alloys [14, 15], carbon-based [16], or metal-oxides [17-20] have all been investigated for their nanofeatures. Due to these new properties at the nanoscale, treatments for bacterial infections have been developed. For example, gold (Au) [12] and silver (Ag) nanoparticles (NPs) [13] have been used to this aim and have shown great results. These chemical elements present naturally antimicrobial and anticancer activity with a low associated cytotoxicity [21, 22]. These great results are not without drawbacks. Au and Ag are rare elements with abundances of 0.004 and 0.075 mg/kg in the Earth's crust [23], respectively. Consequently, their price is around 44800 and 521 USD/kg [23], respectively; see Figure 1. Therefore, any antibacterial treatment based on those expensive chemical elements is not going to be affordable to everybody. This brings the question: are there any materials that could be used widely in the

community achieving similar antibacterial results and being affordable? Some reports have used chemical elements such as selenium (Se) [24] and tellurium (Te) [25], and although being cheaper than gold and silver, they are still relatively expensive (21.4 and 63.8 USD/kg) [23]. Furthermore, these elements are extensively used in solar cell and electronic industries which is keeping their price in the higher end. That is why the American Physical Society and the Materials Research Society have labelled these elements as Energy Critical Elements.

However, bismuth (Bi) seems to be an element of choice for biomedical applications [26, 27]. Many studies have demonstrated its applications in radio-sensing [28] due to their high density which allows for better contrast imaging. When oxidized, bismuth forms bismuth (III) oxide, Bi_2O_3. known for its applications in electronics [29], photo-catalysis [30-35], medicine [36, 37], gas sensing [38], water purification [34], and γ-ray shielding [39]. As a photo-catalyst, Bi_2O_3 has been tested to photodegrade rhodamine B [33], methyl orange [30], rhodamine 6D, and other various water pollutants [34]. In medicine, α-Bi_2O_3 coated with (3-aminopropyl)trimethoxysilane and methotrexate were shown to enhance radio-sensitizing features in dose enhancement radiation therapy [37]. It was shown by Stewart *et al* [36] that α-Bi_2O_3 NPs have high radio-sensitizing capacity. Additionally, it was also shown that Bi_2O_3 is biocompatible [40]. Beside those properties, Bi_2O_3 is a p-type semiconductor and polymorph material that exhibits six different crystal phases: α is monoclinic [41], β is tetragonal [42], γ is body-centered cubic [43], δ is face-centered cubic [44], ε is orthorhombic [45], and ω is triclinic [46]. Each of these crystalline phases exhibits very distinct physico-chemical properties that allow for different potential applications, see Table 1. At room temperature, the most stable and common crystalline phase for Bi_2O_3 is the α-phase.

Several methods have been proposed to synthesize Bi_2O_3 nanostructures of various sizes and shapes. These methods include: oxidative metal vapor transport deposition [47], sol-gel methods [48, 49], wet-chemical synthesis [50], and pulsed laser ablation in liquids (PLAL) [17-20, 26, 27]. Of these methods, PLAL is the most extreme. Most of the PLAL studies on Bi_2O_3 nanomaterials have been performed using lasers operating at low laser repetition rates and low laser fluence; consequently, they synthesized spherical NPs [17-20, 26, 27, 51-53]; see Table 2. Only one PLAL study, completed by Rosa *et al.*[52], was done at a higher repetition rate of 1.5 kHz with an ablation time of 2 minutes. It is the only study that has been completed at a high repetition rate, but the authors did not report the laser fluence or the power of the laser. The laser repetition rate strongly influences the final size and shape of the nanostructures due to the re-irradiation of the nanostructures floating within the colloidal solution during the synthesis. Those multiple irradiations induce fragmentation of the particles already produced by crossing the beam multiple times after their initial synthesis. By increasing the repetition rate, the concentration of particles within the solution also increases until the repetition rate is fast enough that the beam starts hitting the cavitation bubble formed during the previous irradiation [54]. Another important parameter to consider is the target. Indeed, the initial starting shape of the target (powder or pellets) also influences the final size of the NPs [55].

Most recently, Dadashi *et al* [26] was able to combine PLAL of Bi-based-NP with a post process treatment coating them with gold for biomedical applications. Another recently published PLAL study detailed a new type of synthesis protocol called Sonication Assisted-PLAL (S-PLAL), where without sonication the group was able to synthesize Bi-based nano-spheres as with standard PLAL, but with sonication (S-PLAL) they were able to synthesize Bi-based nano-sheets [18].

To the best of our knowledge, herein we present for the first time the synthesis of Bi_2O_3 nanoflakes (Bi_2O_3NFs) by PLAL without any external field assistance (no acoustic, electric or magnetic field). This work includes characterization of these nanoflakes by UV-visible spectroscopy (UV-vis), Atomic Emission Spectroscopy (AES), Transmission Electron Microscopy (TEM) with Energy Dispersive Spectroscopy (EDS), Selected Area Electron Diffraction (SAED), X-ray Photoemission Spectroscopy (XPS), Atomic Force Microscopy (AFM), Scanning Electron Microscopy (SEM), Raman Spectroscopy, and Photoluminescence Spectroscopy (PL). After complete characterization, the nanostructures have been tested for their biomedical applications as antimicrobial agents, towards both Gram negative and positive antibiotic-resistant strains, and as an anticancer active component against melanoma cells while remaining biocompatible for human healthy skin cells.

2. Methods

2.1. Synthesis of Bi_2O_3NFs

A single bismuth needle of 99.97% purity from Alfa Aesar [LOT: N27E043] was placed at the bottom of a flat cylindrical beaker (Pyrex) and was covered with 7 mL of molecular biology grade de-ionized water (DI H_2O) from Alfa Aesar [LOT: 177910]; see Figure 2a. The needle was then irradiated by a Q-Switched Nd:YAG laser from Electro Scientific Industries emitting in the infrared region at 1064 nm. The laser beam was reflected by a flat mirror angled at 45° with respect to the laser rail and then directed through an 83 mm lens which focused the beam onto the bismuth needle submerged in DI water. The beam size diameter at the surface of the target was measured to be around 100 μm. The laser power was measured in continuous mode to be 12.5 W. This gives

a fluence of 159 J/cm^2. The irradiation lasted for 5 minutes at a repetition rate of 1 kHz. The laser beam was hitting the same spot on the target during the entire duration of synthesis. After irradiation, the target (bismuth needle) was removed from the solution, which was dark brown in color, and a tiny dark spot was observed at the surface of the needle revealing the presence of the ablation crater.

2.2. Material Characterization

After irradiation, the solution was poured into a 5 mL opaque plastic microtube for storage and further analysis. The solution was first analyzed by UV-vis (Shimadzu UV-3600 UV/Vis/NIR Spectrometer) and AES (AES, MP-4210 from Agilent). A droplet of the colloidal solution was then placed onto a silicon wafer for SEM analysis within a JEOL JSM7000F microscope. AFM (Bruker Icon AFM) was performed in tapping mode using a silicon AFM probe from Ted Pella, Inc [Prod No. TAP300-G-10] with a resonant frequency of 300 kHz and a force constant of 40 N/m. A droplet was placed onto a carbon film copper grid for analysis by TEM performed in the JEOL JEM2100F and the JEOL ARM200F microscopes operated at 80 kV and 200 kV, respectively. The crystalline structure has been analyzed by SAED patterns. Off-axis electron holography has been performed to determine the thickness of the samples and compared with AFM measurements. In the optical measurement procedure (Raman spectroscopy + PL), nano-flakes were first drop-casted onto a Si substrate. The sample was optically excited by an ultrafast laser (Coherent Chameleon Ultra II, 80 MHz, 150 fs) at 395 nm for PL measurements and by a 633 nm continuous wave laser for Raman detection. The excitation spot and average power were ~ 2 μm / 200 μW for 395 nm laser, and 0.42 μm / 1 mW for 633 nm laser, respectively. The PL or Raman signal was filtered by appropriate long-pass filters, analyzed by a spectrometer (Horiba iHR550)

and detected by a Charged-Coupled Device (CCD) camera. For XPS measurements, a drop of colloidal solution was placed onto a silicon wafer and then processed into a Thermo K-Alpha XPS. All samples were prepared for analysis just after the synthesis was completed.

2.3. Biomedical Characterization

2.3.1. Antimicrobial assays

Two different strains of bacteria were tested for antimicrobial properties using the Bi_2O_3NF: one Gram-negative bacteria (multidrug-resistant *Escherichia coli* (MDR-EC) (ATCC BAA-2471; ATCC, Manassas, VA) and one Gram-Positive bacteria (Methicillin-resistant *Staphylococcus aureus* (MRSA) (ATCC 4330; ATCC, Manassas, VA)) were utilized for the antibacterial tests. The cultures were kept on agar plates at 4 °C.

Colony counting unit assays were completed by seeding the bacteria in a 96-well plate mixed with different concentrations of Bi_2O_3NF. The plates were incubated at 37 °C for 8 h; after that period of time, they were removed from the incubator and diluted with PBS in a series of vials by $\times 10^4$ $\times 10^5$ and $\times 10^6$. Three drops of 10 µL were taken of each dilution and deposited on an LB agar plate. The plates were deposited inside an incubator at 37 °C until the colonies grew enough without reaching confluency. Afterward, the numbers of colonies formed were counted, and the data was processed.

2.3.2. Cytotoxicity assays

Cytotoxicity assays were performed with primary human dermal fibroblast cells (Lonza, CC-2509, AMP) and melanoma cells (ATCC® CRL-1619, Manassas, VA). The cells were cultured in

Dulbecco's Modified Eagle Medium (DMEM; Thermo Fisher Scientific, Waltham, MA), supplemented with 10% fetal bovine serum (FBS; ATCC® 30-2020™, American Type Culture Collection, Manassas, VA) and 1% penicillin/streptomycin (Thermo Fisher Scientific, Waltham, MA). Cells were seeded onto tissue-culture-treated 96-well plates (Thermo Fisher Scientific, Waltham, MA) at a final concentration of 5000 cells per well in 100 µL of cell medium. After an incubation period of 24 h at 37 °C in a humidified incubator with 5% carbon dioxide (CO2), the culture medium was replaced with 100 µL of fresh cell medium containing increasing concentrations of different nanoflakes. Controls containing either cells and media or just media were included in the 96-well plate to identify the average growth of cells without the NPs and determine the absorbance of the media. Cells were cultured for 24h or 72h in the same conditions, followed by washing with PBS and replacing the medium with 100 µL of MTS (3-(4,5-Dimethylthiazol-2-yl)-5-(3-carboxymethoxyphenyl)-2-(4-sulfophenyl)-2H-tetrazolium, CellTiter 96® Aqueous One Solution Cell Proliferation Assay, Promega, Madison, WI) solution (mixing ratio of 1:5 of MTS:medium) which was used to assess the cells' metabolic activity. After the addition of the solution, the 96-well plate was incubated for additional 4h to allow for a color change. Then, the absorbance was measured at 490 nm on an absorbance plate reader (SpectraMAX M3, Molecular Devices). Cell viability was calculated by dividing the average absorbance obtained for each sample by the one obtained for the control sample and then multiplied by 100.

2.3.3. Reactive Oxygen Species (ROS) assays

For ROS quantification, 2′,7′-dichlorodihydrofluorescein diacetate (H2DCFDA) was used. Human melanoma cells were seeded in a 96 well-plate at a concentration of 5 × 104 cells/mL in DMEM

medium, with addition of different concentrations of NPs (from 0 in control and up to 100 μg/mL). The cells were cultured under standard culture conditions (37 °C in a humidified incubator with a 5% carbon dioxide (CO2) atmosphere) for 24 h before the experiment. Briefly, the ROS indicator was reconstituted in anhydrous dimethylsulfoxide (DMSO) to make a concentrated stock solution that was kept and sealed. The growth media were then carefully removed and a fixed volume of the indicator in PBS was added to each one of the wells at a final concentration of 10 μM. The cells were incubated for 30 min at optimal temperature and the loading buffer was removed afterwards. Fresh media was added and cells were allowed to recover for a short time. The baseline for fluorescence intensity of a sample of the loaded cell period exposure was determined. Positive controls were done by stimulating the oxidative activity with hydrogen peroxide to a final concentration of 50 μM. The intensity of fluorescence was then observed by flow cytometry. Measurements were taken by an increase in fluorescence at 530 nm when the sample was excited at 485 nm. Fluorescence was also determined in the negative control, which were untreated cell loaded with dye and maintained in a buffer.

2.3.4. Statistical Tests

All biological experiments were repeated in triplicate (n = 3) to ensure the reliability of the results. Statistical significance was assessed using Student's t tests, with a $p < 0.05$ being statistically significant. Results are displayed as mean ± standard deviation.

3. Results

3.1. Effect of Laser Fluence on Morphology

In order to better understand the effect of the laser fluence on the production of nanostructures by PLAL, a series of synthesizes were completed at ~32, 95, and 159 J/cm^2; see Figures 2a, 2b, and 2c, respectively. From the SEM images, it is clear that at low laser fluence (Figure 2a), a mixture of nanospheres and nanoflakes were synthesized. As the laser fluence was increased, Figures 2c and 2d, the spherical population was removed from solution and the nanoflakes were the only population observed. Besides the elimination of nanospheres, another effect was noticed, in that the nanoflakes morphology became well defined as small squares. This morphology is totally unusual for the PLAL synthesis technique. Consequently, the nanoflakes synthesized at ~159 J/cm^2 were selected as the focus of the paper.

3.2. Physico-chemical characterization

The colloidal solution was first characterized by UV-vis (Figure 2d). The solution was initially a dark brown color; see inset Figure2d, and after a short time changed into a yellow-white color. The normalized absorbance spectrum is displayed in Figure 1b. The observed dark brown color of the colloidal solution containing the bismuth-based nanostructures was in agreement with previous observations [17-19, 26, 27, 51, 52]. The strongest absorbance within the UV-vis spectra was obtained in the UV region, at 312 nm (i.e. 3.97 eV), which corresponds to the highest absorption peak, named λ_{max}. The concentration of the colloidal solution, c, has been determined independently by AES to be around 89.5 ± 4.3 ppm i.e. it corresponds to a molarity of (1.9 ± 0.1) x 10^{-4} M. Therefore, by using the Beer-Lambert's law (valid at concentration below 0.01 M), $A = \varepsilon l c$, where A is the absorbance and l is the path length of light through the cuvette, and ε is the molar extinction coefficient (also called molar absorptivity) which is determined to be (4.1 ± 0.2) x 10^3 $M^{-1}cm^{-1}$. This is an intrinsic property of the bismuth-based species contained in the colloidal

solution and it is a measure of how strongly they absorb light at 312 nm. This value is found to be comparable with the molar extinction coefficient of other bismuth compounds i.e. 6.501 x 10^3 $M^{-1}cm^{-1}$, obtained for bismuth(III)-1 amino trimethyl pyrimidine thiol [56], 1.77-6.36 x 10^3 $M^{-1}cm^{-1}$ Bi (III)-ethylene diamine di hydroxypropionic acid [57].

From the Tauc relationship [58], which is given as: $(\alpha . h\nu)^m = h\nu - E_g$; where $h\nu$ is the photon energy, m being the index characterizing the type of transition (direct or indirect) and α is the absorption coefficient that can be calculated from the absorbance measured by UV-vis spectroscopy. The energy bandgaps, E_g, were calculated to be 1.88±0.01 eV and 2.53±0.01 eV which seems to correspond to the γ- and α- phases, respectively (Table 1). In Figure 2e, the graph of $(\alpha . h\nu)^m$ versus the photon energy, $E = h\nu$ was plotted. The extrapolation of a straight line to the x-axis, $(\alpha E)^2 = 0$, gives the value of a direct band gap ($m = 1/2$), while, the extrapolation of a straight line to $(\alpha E)^{1/2} = 0$ gives the value of an indirect band gap. Figure 2e supports the existence of two direct bandgap materials. Figure 2f shows the PL spectra acquired at room temperature from an ensemble of Bi_2O_3 nano-flakes. At room temperature, the emission spectrum from nano-flakes exhibits a broad band from 450 nm to 700 nm. It is also worth to mention that in our measurements the spectral range below 420 nm could not be detected due to the low efficiency of a silicon CCD camera. This broadness is due to a mixture of both α- and γ-phases. Therefore, the broad peak was fitted by using two Gaussian curves as indicated in Figure 2f. The two peaks correspond to energies bandgap of 1.80±0.06 eV and 2.14±0.01 eV, respectively.

In order to determine the morphology and chemical nature of the structures within the colloidal solution, TEM and additional SEM were performed. Figure 3a and 3b, show low magnification

TEM and SEM images of the structures after being drop-casted onto a copper grid and silicon wafer, respectively. From these observations, the "flake" morphology is determined. Figure 3c shows a typical STEM image of the bismuth-based flakes. EDS was performed in order to identify the chemical nature of the flake. From the EDS analysis, the flake is made of bismuth and oxygen, as expected from the ablation process. Figures 3d, 3e, and 3f show the mapping of bismuth, oxygen, and bismuth plus oxygen, respectively. Bismuth and oxygen can combine according various stoichiometric ratio (1:1, 2:3, 2:5), so to confirm the exact stoichiometric ratio of the bismuth oxide flakes obtained by PLAL, XPS was performed (Figures 3g and 3h). The Bi4f7 scan revealed a peak centered about 159 eV which has been attributed to the Bi-O bond corresponding to Bi_2O_3. The Bi4f5 scan revealed a peak centered about 165 eV which is also a peak that has been attributed to the Bi-O bond corresponding to Bi_2O_3. There are no peaks centered about 157 eV or 162 eV which are attributed to the Bi-Bi bond [59]. In figure 3f, there is another peak centered on ~531 eV which is commonly attributed to metal oxides. This further confirms the 2:3 stoichiometric ratio of our flakes. So clearly, Bi_2O_3 is the material compound constituting the surface of the flakes.

Raman spectroscopy was performed and confirmed the presence of α- and γ- phases of Bi_2O_3 (Figure 3i). Figure 3i displays the Raman spectra from several Bi_2O_3 nano-flakes at room temperature. These nano-flakes exhibited several distinguishable Raman peaks which were identified as α- Bi_2O_3 (123, 141, 154, 186, 213, 278, 315, 411 and 450 cm^{-1}) and of γ- Bi_2O_3 (163 and 249 cm^{-1}). From the Raman spectra, α- Bi_2O_3 peaks dominate as reported previously [60, 61]. Due to the limitation of the long-pass filter, we could only detect Raman peaks which have wavenumbers higher than 100 cm^{-1}. The 123 cm^{-1} mode is coming from Ag symmetry caused by

mainly the Bi atoms' participation. Modes of 141 (A_g) and 154 cm^{-1} (B_g) may come from the displacements of both Bi and O atoms in the α-Bi_2O_3 lattice. The Raman peaks of the higher frequency modes 186, 213, 278, 315, 411, 450 cm^{-1} are attributed to the displacements of the O atoms in α-Bi_2O_3 [62].

The chemical composition of the surface of the flakes performed by XPS confirmed the formation of Bi_2O_3, and a mixture of α- and γ- phases were indicated by Raman spectroscopy; however, further studies were necessary in order to determine the crystallinity of the flakes. Indeed, Bi_2O_3 has six different allotropes and they each have their own distinct physico-chemical properties (Table 2). To determine the phase of bismuth oxide synthesized by PLAL, SAED was performed (Figure 4). From figure 4b, the indexed SAED pattern corresponds to the α- Bi_2O_3 phase. Moreover, γ- Bi_2O_3 phase commensurate structures have also been found (Figure 4c and 4d) [63, 64]. The crystalline phases experimentally determined by electron diffraction is performed by finding the zone axis, and subsequently by measuring the reflections of the electron diffraction pattern, and by comparing the distances of the reciprocal lattice of the possible phases. However, despite the consideration of forbidden reflections produced by dynamical interaction, when some reflections (typically weak spots) do not correspond with the expected Bragg diffraction spots and when a simple fraction of the periodic arrangement is identified, i.e. (1/2,0,0); then, the atomic distribution can present commensurability. In the analysis performed by electron diffraction, commensurate structures of the γ-phase is measured and shown in Figures 4c and 4d. Commensurability has already been observed in Bi_2O_3 by Zhou *et al* [64]. Figure 4e shows a high resolution TEM (HRTEM) image in which the fast Fourier transform present a commensurate pattern as can be observed in the modulation contrast of the dark field image in Figure 4f.

Since the x- and y- dimensions are micron-size i.e. well beyond the typical length and width scale to be considered nanostructures, AFM characterization was performed to determine the thickness of the flakes (Figure 5a). AFM measurement revealed an average thickness of 50 nm. For thickness determination of the flakes by electron holography, we have configured a field of view of 4 microns at 42V of the bi-prism excitation and a fringe contrast of about 25%. Figures 5b and 5c show the hologram and the reconstructed phase, respectively. Reconstructed phase of the hologram indicates a phase shift (Δφ) related to the thickness (τ), which is calculated using $\Delta\varphi = C_E|V_0|\tau$, where V_0 represents the mean inner potential for α-Bi_2O_3 (9.35 V), calculated using the atomic scattering amplitudes from Ref. [65], and the parameter C_E is 0.00729 rad/V nm for the 200 kV accelerating voltage. Thickness measured by electron holography, after carbon background subtraction (~20 nm of a lacey carbon commercial grid) was ~68 nm as shown in Figure 5d. Since our average thickness is below 100 nm, those structures are nano-flakes.

3.3. Antimicrobial assays

Colony counting assays are performed using one gram positive, MRSA, and one gram negative, MDR-EC. The results, Figure 6, show different results for either the gram positive or negative samples. Between the two, the gram negative sample shows the greatest antibacterial effect. It is also clear that the minimum inhibitory concentration (MIC) for them was estimated between 5-10 ppm and 0-5 ppm Bi_2O_3NF's for the gram positive and negative bacteria, respectively. This suggests that the Bi_2O_3NF's are more effective at inhibiting the growth of gram negative bacteria. These reported MIC values are significantly lower than those reported in literature: for instance, Campos *et. al.* reported a MIC value of 267 ppm for exposure of bismuth oxide NPs to *Escherichia*

coli and *Staphylococcus aureus* [66]. Besides, these experimental results are in concordance with the fact that bismuth oxide NPs can inhibit the growth of drug resistant pathogens[67], although this article successfully reported for the first time the inhibition of the antibiotic resistant pathogens MDR *Escherichia coli* and MRSA.

3.4. Cytotoxicity assays

To determine the cytotoxicity of the Bi_2O_3NFs on mammalian cells, in vitro MTS assays were performed with human dermal fibroblasts (HDF) and human melanoma cells using different nanoflakes concentrations, ranging from 10 and 50 µg/mL for between 24 and 72 hours (Figure 7). As shown in the figure, no significant cytotoxicity towards HDF cells was found for the whole range of concentrations at 24h, showing no statistical differences compared to the control. Furthermore, a 72h treatment led to the same cytotoxicity trend, except for the highest concentration, were there was a slight deviation compared to the control, indicating that such treatment conditions might not be the best option for a 72h cell exposure. On the other hand, when melanoma cells were exposed to Bi_2O_3NF at the same concentration range, both 24 and 72h treatments led to significant decays in cell proliferation, even at the lowest concentration. Moreover, when exposed to concentrations of 15 µg/mL and higher, the cell decay was larger than 50%, with no cell growth observed beyond that point at 25 and 50 µg/mL. Consequently, exposure of human cells to Bi_2O_3NF render a good biocompatibility in the range 5 to 25 µg/mL for 72h treatment, while an important anticancer effect is shown at the same range.

These results open the window for a potential external use of the nanoparticles for melanoma treatment. Some studies have demonstrated that Bi2S3 NPs [68] are internalized by cells via endocytosis, and in some cases the former have been found ‘clustered’ around the membrane

within the cytoplasm. Therefore, the NPs are expected to be internalized and enclosed inside the cells, which might be used for an enhancement of radiation therapy, as was shown by Algethami *et al.* who demonstrated that bismuth-based nanoformulations would a cheaper viable alternative to the use of other noble metal nanoparticles as effective dose enhancing agents when used in clinical applications [69]. Furthermore, the NPs presented in this article could be used in combination with anticancer drugs, such as doxorubicin (DOX) and hydrogels for a quick and sustained released to the malignant tumors, which was demonstrated to achieve significantly synergistic antitumor effects in vitro [70]. Therefore, it is hypothesized that the combination of Bi2O3NF with an injectable macroporous hydrogel may serve as a combinational therapeutic platform for clinical superficial cancer therapy.

3.5. Reactive Oxygen Species (ROS)

The analysis of ROS allowed for the evaluation of toxicity towards human melanoma cells, performed by exposing different concentrations (from 5 to 50 μg/mL) of the Bi_2O_3NFs. After a 24 h treatment, the ROS could be successfully quantified in the cell media. An increase in the production of ROS (Figure 7) was observed when the NPs interacted with the melanoma cells, with a dose-dependent effect. Our results indicated that Bi2O3 NFs induced cytotoxicity in melanoma cells through oxidative stress pathway. Several studies have shown that leaching of ROS from the surface of metal oxide NPs in culture media might play crucial role in cell cytotoxicity, and that the excessive ROS generation can led to DNA damage, genetic mutations and the variable alteration of the expression of different genes associated with apoptosis[71] and other mechanisms of cell death[72]. Bismuth oxide NFs have been reported to elicit an increase in

the ROS production in culture media, which is aligned with the experimental results showed in this report[73, 74].

4. Discussion

4.1. Nanoflake formation mechanism

Now that the 2D structure of the nanostructures has been established, it is important to understand their growth process. Laser exfoliation of the target was considered as a possible growth mechanism, but due to the chemical nature of the flake, Bi_2O_3, the formation of bismuth oxide cannot be explained by exfoliation (i.e. exfoliation of a pure bismuth target should result in pure bismuth nanoflakes, not Bi_2O_3 nanoflakes) [75]. Therefore, another growth mechanism was considered. PLAL is a straightforward physical technique to produce nanostructures. The laser beam interacts with the pure bismuth target while it is submerged in DI water. The target and the solvent get ionized and it consequently creates a plasma made of electrons, bismuth ions, hydrogen ions, and oxygen ions. Then, when the beam is off, the plasma cools down and releases the heat to the surrounding solvent creating a cavitation bubble. Within this cavitation bubble, the ions start reacting together forming bismuth oxide compounds. Bismuth oxide adopts a 2D growth in order to minimize the energy of its overall structure by privileging the growth of low surface energy facets [76]. In this case, there are two competing factors, one geometric that minimizes the surface to volume ratio and one energetic that minimizes the surface energy. When the surface energy of the compound is below the surface energy of the solvent then the energetic factor wins and allow the structure to grow like a 2D material. When it is the contrary the structure adopts a spherical morphology in order to minimize the surface to volume ratio. The surface energy of Bi_2O_3 was recently measured by the Zisman method (i.e. the surface energy of the solid is the surface energy

at which a liquid just completely wets the solid) to be 31.95 x 10^{-3} J/m^2 which is obviously much less than the surface energy of water, 72.80 x 10^{-3} J/m^2 [77, 78].

4.2. Cost Analysis

To bring this nanostructure to market, cost can ultimately be the breaking point for its use by the general public. In terms of nanoparticle treatments, the materials used are often expensive (gold and silver) and here we provide discussion surrounding the cost in USD per ppm of treatment to achieve bacterial proliferation. Figure 8 shows the cost of the nanoparticle treatment for various bacteria for various material systems versus its MIC value. We made no distinction between gram-negative or positive bacteria and no distinction between shapes or sizes of the NPs. We see pretty clearly in this analysis that gold and silver nanoparticle treatments are very expensive to reach the MIC value for any bacteria while other cheap alternatives are available like TiO_2 or ZnO. We also included our Bi_2O_3NF's data in this analysis and find that it was very cost effective, which demonstrate that the nanostructures produced in this work are a cost effective antibacterial nanoparticle treatment.

5. Conclusions

Bi_2O_3 nano-flakes have been successfully synthesized by PLAL at high fluence (~159 J/cm^2) without any external assistance like acoustic, electric or magnetic fields. The nano-flakes exhibited two different phases: α- and γ- (commensurate structure). The physical dimensions of the flakes were several microns long along the x- and y- axis while only ~50 nm thick along the z-axis. The strongest advantage of using PLAL as a synthesis methodology is the cleanliness of the Bi_2O_3's surface. More work is required to finely tune the irradiation time, the fluence and the repetition

rate in order to control more precisely the crystalline structure, and thickness of the Bi_2O_3 nano-flakes. The nanoflakes are also revealed a cost effective antibacterial treatment for the gram-positive and negative bacteria tested in this report, MSRA and MDR E. coli, while remaining biocompatible in the same concentration range. Moreover, the nanostructures showed a dose-dependent and sustained anticancer effect over time with a ROS-related mechanism of cell-death, which suggest that this technology might be used for a superficial application in the treatment of cancer such as melanoma.

Acknowledgements.

L. D. G., M. K. and G.G. would like to thank the Center for Integrative Nanotechnology Sciences (CINS) of UA Little Rock for the use of their UV-vis, AFM, SEM and TEM. Dr. Fumiya Watanabe (UA Little Rock, CINS) is greatly acknowledge for his help acquiring the XPS spectra. Y. A. and T. B. H. acknowledge the financial support from the National Science Foundation (NSF) (Grant # DMR-1709612). P. P. and A. P. thanks the Kleberg Advanced Microscopy Center at UTSA and DoD financing support #W911NF-18-1-0439.

Table 1. Bismuth oxide (Bi_2O_3) physico-chemical properties.

Phase	Crystal structure	Lattice parameters			Energy bandgap (eV)	Applications	Ref.
		a (A)	b (A)	c (A)			
α	monoclinic	5.848	8.166	7.510	2.8	Photo-catalysis	[41], [32], [33]
β	tetragonal	7.730	--------	5.630	2.5	water purification, photo-catalysis	[42], [32], [34]
γ	b.c.c.	10.268	--------	--------	1.9	•	[43]
δ	f.c.c.	5.644	--------	--------	1.7 – 2.0	fuel cells, electronics	[44, 79]
ω	triclinic	4.956	5.585	12.730	•	•	[46]
ε	orthorhombic	7.269	8.639	11.970	•	•	[45]

- Not reported

Table 2. Bismuth oxide (Bi_2O_3) nanostructures by PLAL.

Group	Laser Parameters					Target Parameters			Products	Ref
	Laser Type	**f (Hz)**	**τ (ns)**	**t (min)**	**F (J/cm^2)**	**Target Type**	**Liquid**	**V (ml)**		
Escobar - Alarcon	355 nm Nd:YAG	10	5	10	0.6 - 1.1	99.99% purity Bi disk	DI H_2O	•	α- Bi_2O_3 NPs α, β - Bi_2O_3 NSs	[18]
Gondal	355 nm Nd:YAG	•	•	40	•	99.998% purity Bi Powder	H_2O_2	10	α- Bi_2O_3 NPs	[19]
Dadashi	1064 nm Nd:YAG	10	12	5	118 mJ/ pulse[(a)]	99.99% purity	DI H_2O	60	α, β - Bi_2O_3 NPs	[17]
Ismail	1064 nm Nd:YAG	1	•	200	12	99.99% purity Bi	DI H_2O	•	α- Bi_2O_3 NPs	[20]
Rosa	1064 nm Nd:YAG	1500	200	2	•	99.999% purity Bi pellets	DI H_2O	4	Bi NPs	[52]
This work	1064 nm Nd:YAG	1000	100	5	159	99.97% purity Bi rods	DI H_2O	7	Bi_2O_3 NSs	

(a) Given as Energy per pulse

• Not reported

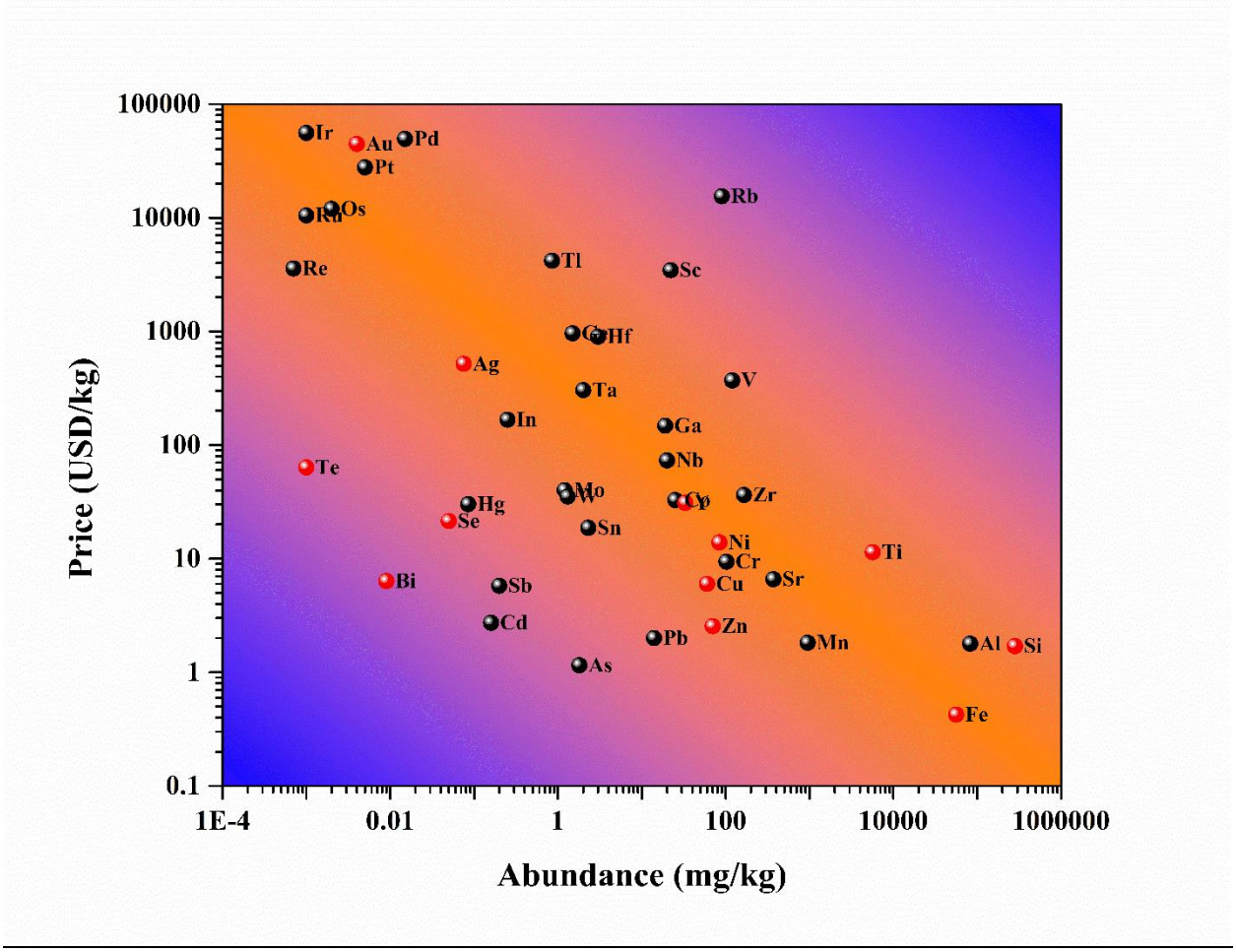

Figure 1. Price of various chemical elements versus their abundance in the Earth's crust. Data were collected from Ref. [23]. The chemical elements highlighted in red are common elements used for biomedical applications.

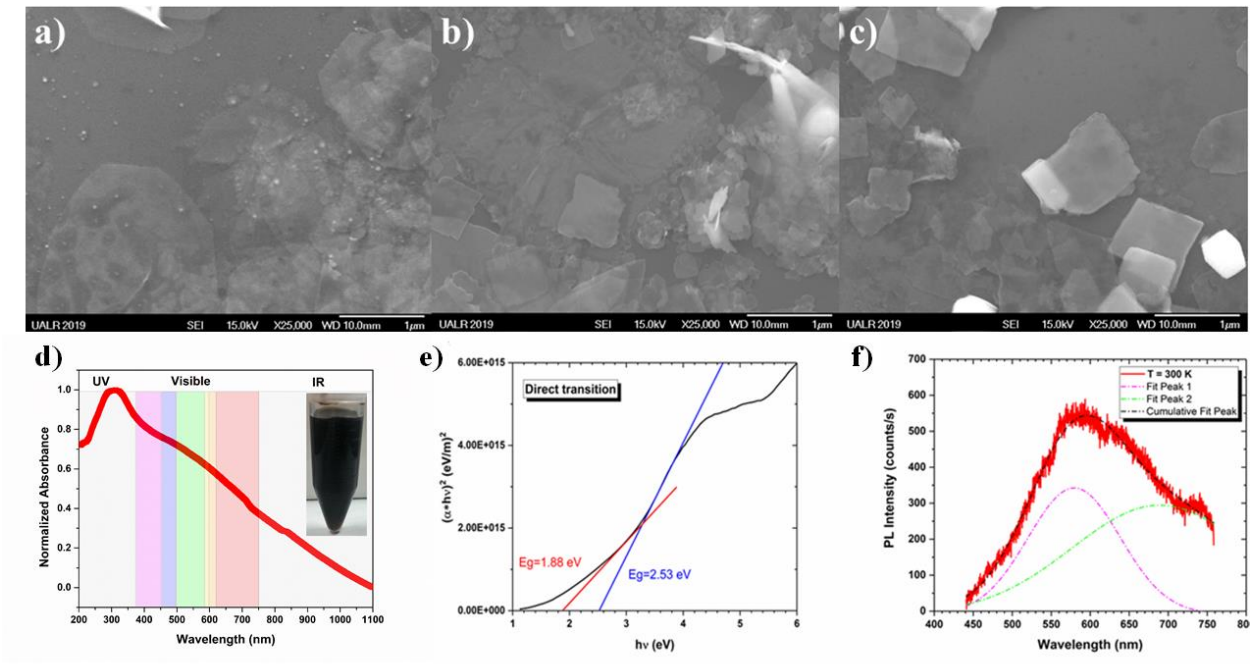

Figure 2. Effect of laser fluence on morphology of nanostrucutres by PLAL ~32 J/cm^2, 95 J/cm^2, and 159 J/cm^2; **a)**, **b)**, and **c)**, respectively. **d)** UV-Vis-NIR spectra of the bismuth oxide colloidal solution synthesized at high fluence (~159 J/cm^2). Inset: Photograph of the colloidal solution just after synthesis. The colloidal solution exhibits a dark brown color, **e)** Tauc plot from UV-vis absorbance acquired in Figure 1d **f)** Photoluminescence spectra performed at room temperature (300K) on the colloidal solution synthesized at high fluence (~159 J/cm^2).

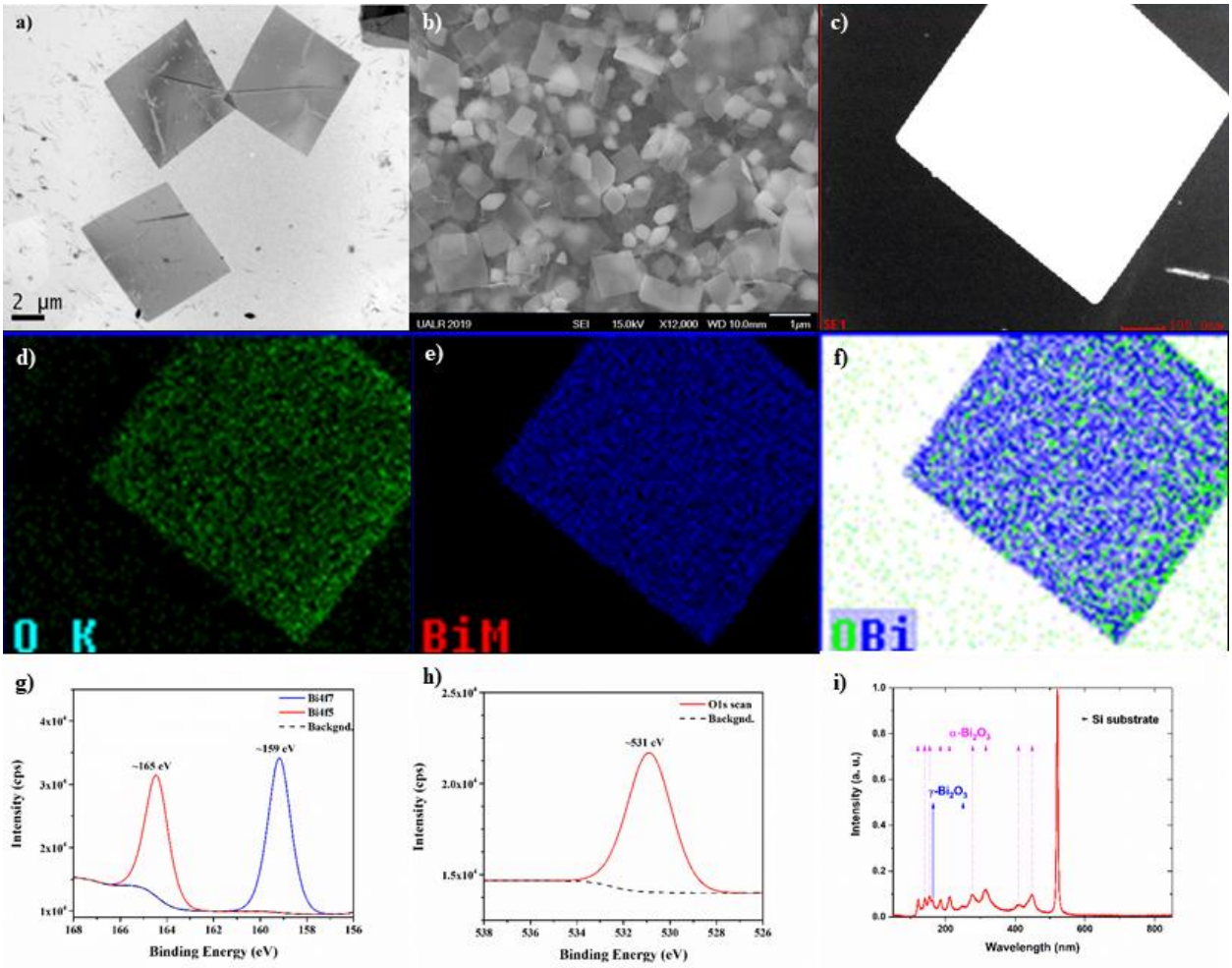

Figure 3 Bismuth oxide flakes obtained at high fluence (159.12 J/cm^2) **a)** Low-magnification TEM image acquired by using the JEOL JEM2100F at 80 kV. **b)** Low Magnification SEM image acquired by using the JEOL JSM7000F at 15 kV. **c)** Typical STEM image of a flake, **d)** Oxygen chemical mapping on the flake, **e)** Bismuth mapping on the flake, and **f)** Chemical mapping displaying the bismuth and oxygen mapping together. The TEM used to acquire those images was the JEOL JEM2100F at 80 kV, **g)** XPS spectra display the bismuth peaks Bi4f7 and Bi4f5 scan, **h)** XPS spectra displaying the oxygen peak, **i)** Raman spectra confirming that two crystalline phases of bismuth oxide (α and γ, see texts for details) are produced during the PLAL synthesis.

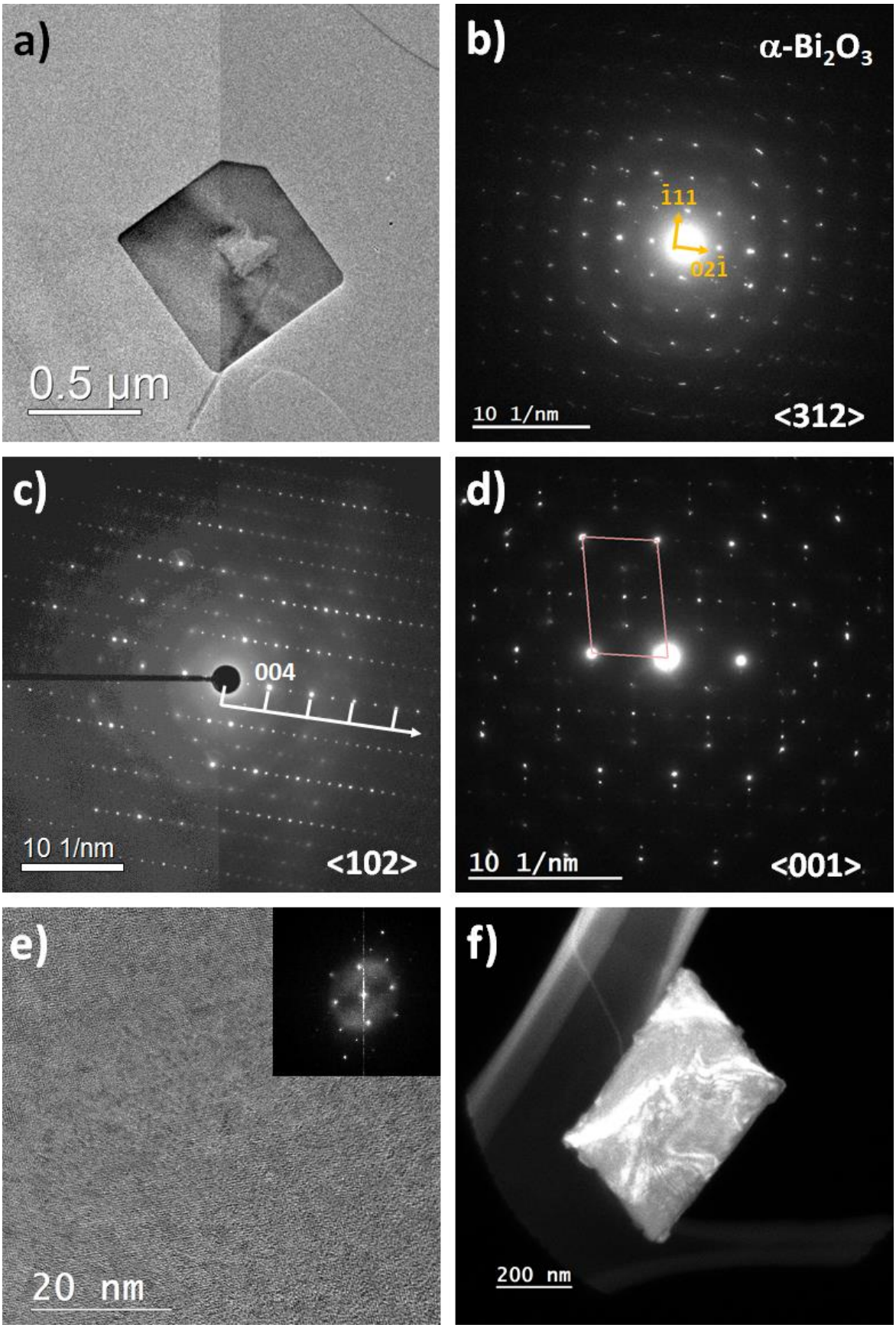
a)
0.5 µm
b)
α-Bi2O3
111
021
10 1/nm
<312>
c)
004
10 1/nm
<102>
d)
10 1/nm
<001>
e)
20 nm
f)
200 nm

Figure 4. Bismuth oxide flake obtained at high fluence (159.12 J/cm^2) **a)** TEM image of an α-Bi_2O_3 nano-flake acquired by using the JEOL ARM200F at 200 kV and **b)** its SAED pattern taken near the <312> zone axis. **c)** and **d)** commensurate structures of the γ-Bi_2O_3 nano-flake recorded in two different zone axes, **e)** HRTEM image of the commensurate γ-Bi_2O_3 structure and **f)** dark field image modulation contrast image.

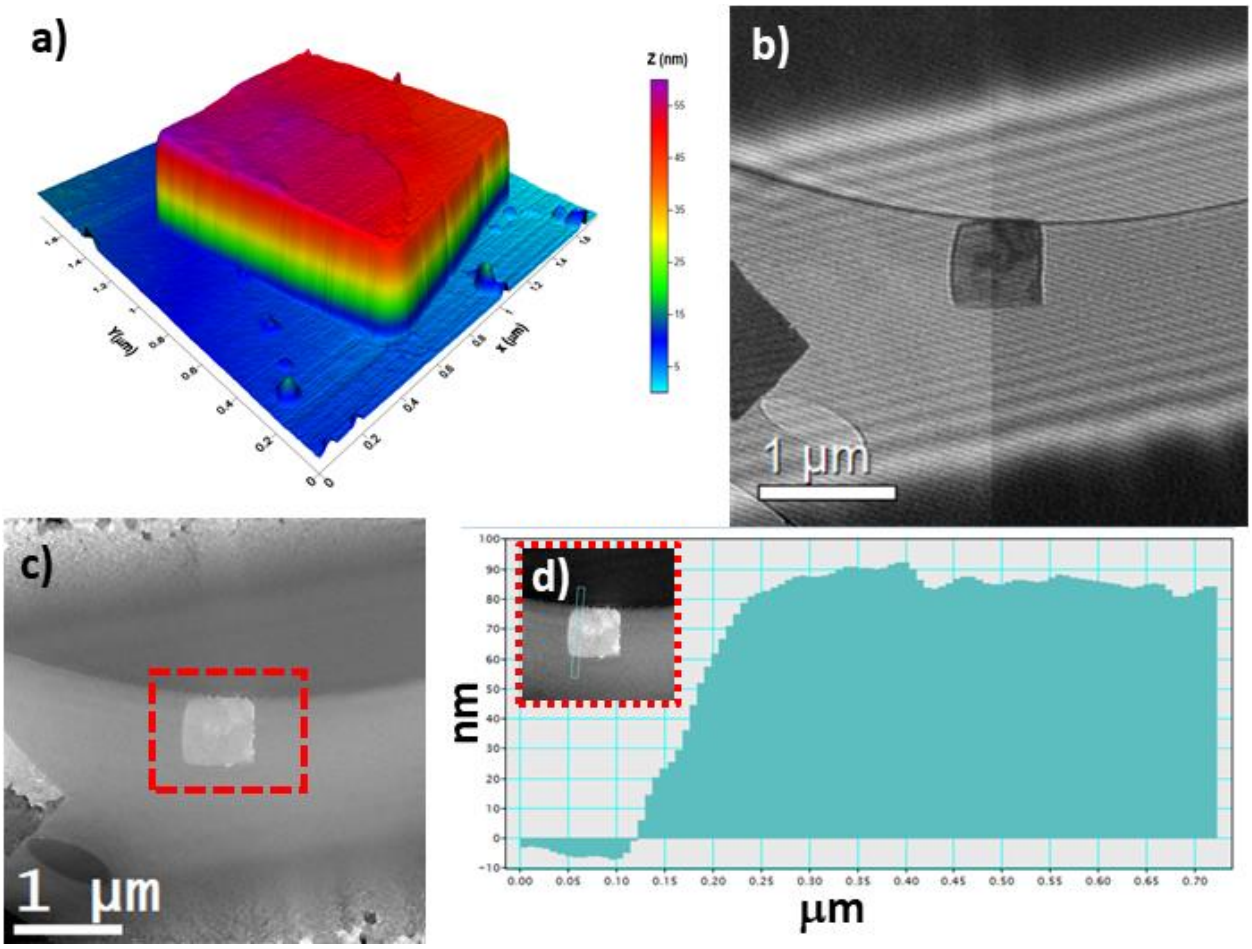

Figure 5. a) AFM image of a Bi_2O_3 flake. Thickness determination by off-axis electron holography performed with the JEOL ARM200F at 200 kV: **b)** electron hologram, **c)** reconstructed phase and **d)** thickness intensity profile after carbon background subtraction ~68 nm.

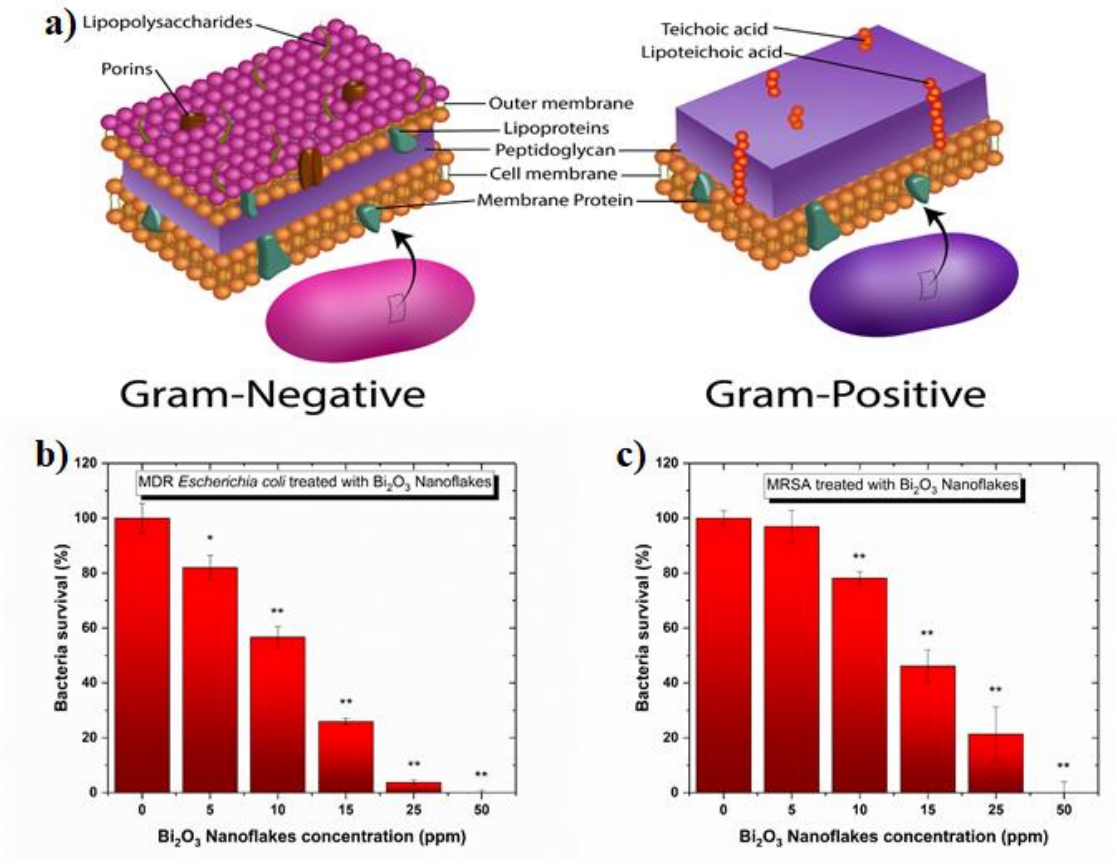

Figure 6. a) Artistic representation showing the internal structure of gram-negative and gram-positive bacteria. Colony counting assay of **b)** MDR E. coli and **c)** MRSA for 8 h in the presence of different concentrations of Bi_2O_3NFs. All values represent the mean ± standard deviation. *p < 0.05, **p < 0.01(compared to controls).

a)

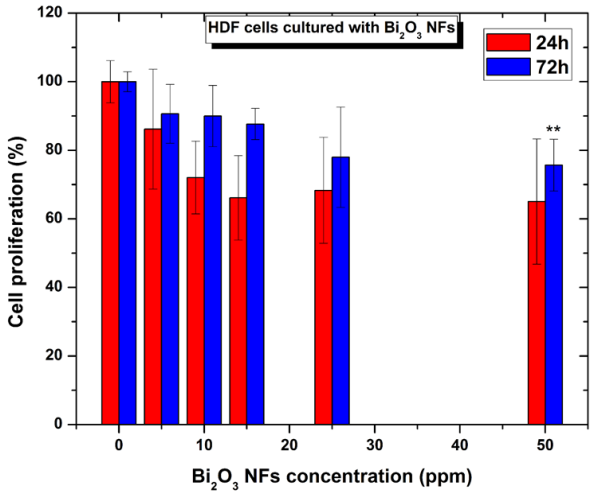
HDF cells cultured with Bi_2O_3 NFs
24h
72h
Cell proliferation (%)
Bi_2O_3 NFs concentration (ppm)

b)

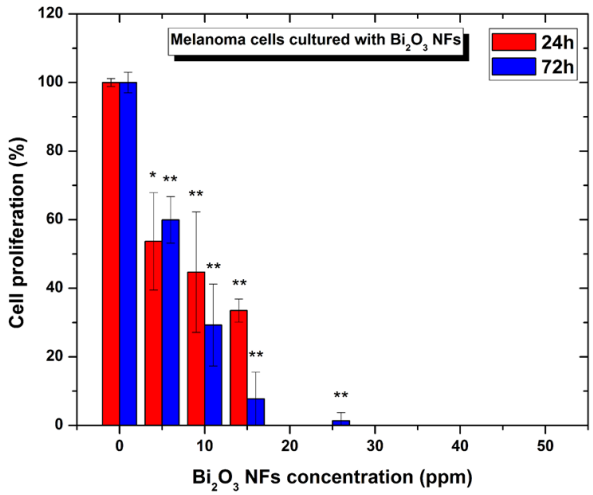
Melanoma cells cultured with Bi_2O_3 NFs
24h
72h
Cell proliferation (%)
Bi_2O_3 NFs concentration (ppm)

c)

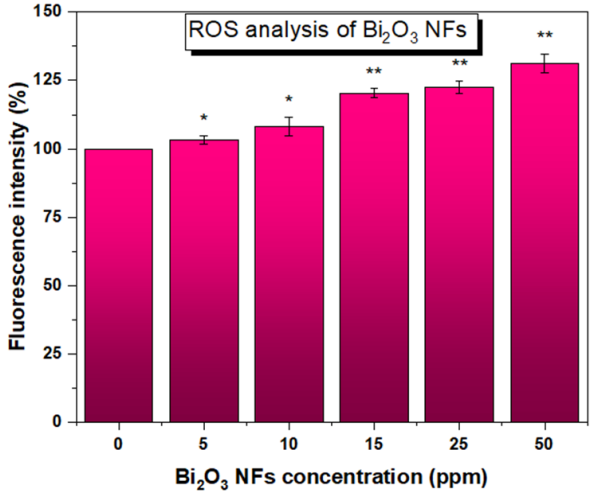
ROS analysis of Bi_2O_3 NFs
Fluorescence intensity (%)
Bi_2O_3 NFs concentration (ppm)

Figure 7. a) HDF, and **b)** melanoma cells in the presence of Bi_2O_3NFs at concentrations ranging from 0 to 50 ppm. n= 3. All values represent the mean ± standard deviation. *p < 0.05, **p < 0.01(compared to controls). **c)** ROS study of Bi_2O_3NFs analysis. n = 3. Data is represented as mean ± SD; *p < 0.05, **p < 0.01(compared to controls).

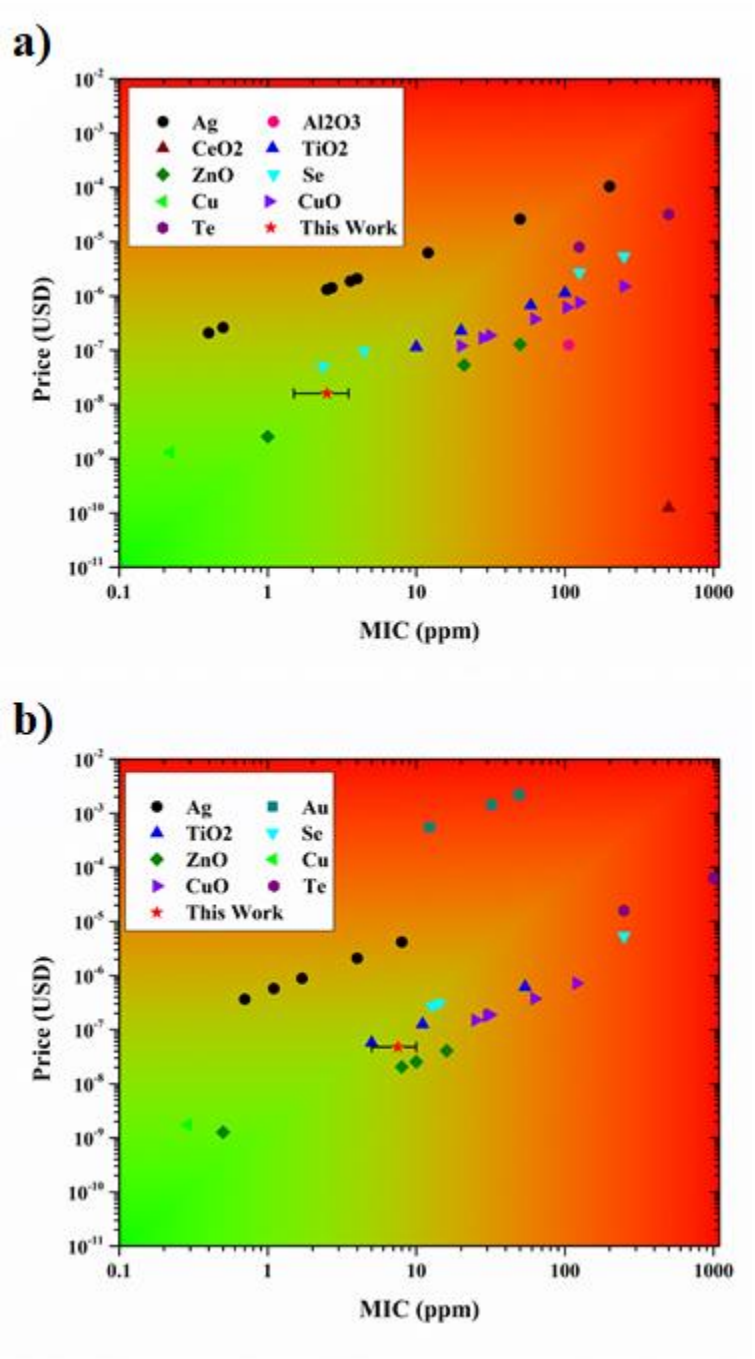

Figure 8. Cost analysis for various antibacterial materials currently used as nanoparticle treatments. Price is the Price of the material/ kilogram multiplied by the MIC i.e., the cost of the treatment. Data were collected from Refs. [24, 25, 80-88].

References

1. Landmarks, A.C.S.I.H.C. *The discovery and development of penicillin*. 1999; Available from: http://www.acs.org/content/acs/en/education/whatischemistry/landmarks/flemingpenicillin.html
2. Aminov, R.I., *A Brief History of the Antibiotic Era: Lessons Learned and Challenges for the Future.* Frontiers in Microbiology, 2010. **1**: p. 134.
3. Organization, W.H.; Available from: https://www.who.int/antimicrobial-resistance/en/.
4. Berry, D., C. Xi, and L. Raskin, *Microbial ecology of drinking water distribution systems.* Curr Opin Biotechnol, 2006. **17**(3): p. 297-302.
5. Cabral, J.P., *Water microbiology. Bacterial pathogens and water.* Int J Environ Res Public Health, 2010. **7**(10): p. 3657-703.
6. Schierholz, J.M. and J. Beuth, *Implant infections: a haven for opportunistic bacteria.* J Hosp Infect, 2001. **49**(2): p. 87-93.
7. Sharma, H., et al., *Metal nanoparticles: a theranostic nanotool against cancer.* Drug Discovery Today, 2015. **20**: p. 1143-1151.
8. Wong, H.L., et al., *Chemotherapy with anticancer drugs encapsulated in solid lipid nanoparticles.* Advanced Drug Delivery Reviews, 2007. **59**: p. 491-504.
9. Lanone, S. and J. Boczkowski, *Biomedical Applications and Potential Health Risks of Nanomaterials: Molecular Mechanisms.* Current Molecular Medicine, 2006. **6**: p. 651-663.
10. Geoffrion, L.D. and G. Guisbiers, *Quantum confinement: Size on the grill!* Journal of Physics and Chemistry of Solids, 2020. **140**.
11. Guisbiers, G., *Advances in thermodynamic modelling of nanoparticles.* Advances in Physics: X, 2019. **4**(1).
12. Elahi, N., M. Kamali, and M.H. Baghersad, *Recent biomedical applications of gold nanoparticles: A review.* Talanta, 2018. **184**: p. 537-556.
13. Marambio-Jones, C. and E.M.V. Hoek, *A review of the antibacterial effects of silver nanomaterials and potential implications for human health and the environment.* Journal of Nanoparticle Research, 2010. **12**(5): p. 1531-1551.
14. Kayal, S. and R.V. Ramanujan, *Anti-cancer drug loaded iron-gold core-shell nanoparticles (Fe@Au) for magnetic drug targeting.* J Nanosci Nanotechnol, 2010. **10**(9): p. 5527-39.
15. Yin, J., et al., *Gold–Copper Nanoparticles: Nanostructural Evolution and Bifunctional Catalytic Sites.* Chemistry of Materials, 2012. **24**(24): p. 4662-4674.
16. Magrez, A., et al., *Cellular toxicity of carbon-based nanomaterials.* Nano Lett, 2006. **6**(6): p. 1121-5.
17. Dadashi, S., R. Poursalehi, and H.H. Delavari, *Formation, gradual oxidation mechanism and tunable optical properties of Bi/Bi2O3 nanoparticles prepared by Nd:YAG laser ablation in liquid: Dissolved oxygen as genesis of tractable oxidation.* Materials Research Bulletin, 2018. **97**: p. 421-427.
18. Escobar-Alarcon, L., et al., *Preparation of bismuth-based nanosheets by ultrasound-assisted liquid laser ablation.* Applied Physics a-Materials Science & Processing, 2016. **122**(4).
19. Gondal, M.A., T.A. Saleh, and Q. Drmosh, *Optical Properties of Bismuth Oxide Nanoparticles Synthesized by Pulsed Laser Ablation in Liquids.* Science of Advanced Materials, 2012. **4**(3-4): p. 507-510.
20. Ismail, R.A. and F.A. Fadhil, *Effect of electric field on the properties of bismuth oxide nanoparticles prepared by laser ablation in water.* Journal of Materials Science-Materials in Electronics, 2014. **25**(3): p. 1435-1440.

21. Jain, S., D.G. Hirst, and J.M. O'Sullivan, *Gold nanoparticles as novel agents for cancer therapy.* Br J Radiol, 2012. **85**(1010): p. 101-13.
22. Le Ouay, B. and F. Stellacci, *Antibacterial activity of silver nanoparticles: A surface science insight.* Nano Today, 2015. **10**(3): p. 339-354.
23. https://en.wikipedia.org/wiki/Prices_of_chemical_elements#cite_note-fn-transient-46. Available from: https://en.wikipedia.org/wiki/Prices_of_chemical_elements#cite_note-fn-transient-46.
24. Geoffrion, L.D., et al., *Naked selenium nanoparticles for antibacterial and anticancer treatment.* ACS Omega, 2020. **5**: p. 2660-2669.
25. Zare, B., et al., *Biosynthesis and recovery of rod-shaped tellurium nanoparticles and their bactericidal activities.* Materials Research Bulletin, 2012. **47**(11): p. 3719-3725.
26. Dadashi, S., R. Poursalehi, and H. Delavari, *Optical and structural properties of oxidation resistant colloidal bismuth/gold nanocomposite: An efficient nanoparticles based contrast agent for X-ray computed tomography.* Journal of Molecular Liquids, 2018. **254**: p. 12-19.
27. Dadashi, S., R. Poursalehi, and H. Delavari, *Optical and structural properties of Bi-based nanoparticles prepared via pulsed Nd:YAG laser ablation in organic liquids.* Applied Physics a-Materials Science & Processing, 2018. **124**(6).
28. Yu, X., et al., *Ultrasmall Semimetal Nanoparticles of Bismuth for Dual-Modal Computed Tomography/Photoacoustic Imaging and Synergistic Thermoradiotherapy.* ACS Nano, 2017. **11**(4): p. 3990-4001.
29. Bandoli, G., et al., *Pure and mixed phase Bi2O3 thin films obtained by metal organic chemical vapor deposition.* Chemical Vapor Deposition, 1996. **2**(6): p. 238-242.
30. Pan, C.Y., et al., *Synthesis of Bismuth Oxide Nanoparticles by a Templating Method and its Photocatalytic Performance.* Advanced Materials Research, 2012. **557-559**: p. 615-618.
31. Farzaneh, F., et al., *Green Synthesis and Characterization of Bi2O3 Nanorods as Catalyst for Aromatization of 1,4-Dihydropyridines.* Journal of Sciences, Islamic Republic of Iran, 2017. **28**: p. 113-118.
32. Lu, Y., et al., *Induced Aqueous Synthesis of Metastable β-Bi2O3 Microcrystals for Visible-Light Photocatalyst Study.* Crystal Growth & Design, 2015. **15**(3): p. 1031-1042.
33. Oudghiri-Hassani, H., et al., *Synthesis, characterization and photocatalytic activity of α-Bi2O3 nanoparticles.* Journal of Taibah University for Science, 2018. **9**(4): p. 508-512.
34. Schlesinger, M., et al., *Metastable beta-Bi2O3 Nanoparticles with Potential for Photocatalytic Water Purification Using Visible Light Irradiation.* ChemistryOpen, 2013. **2**(4): p. 146-55.
35. Hameed, A., et al., *Surface phases and photocatalytic activity correlation of Bi2O3/Bi2O4-x nanocomposite.* J Am Chem Soc, 2008. **130**(30): p. 9658-9.
36. Stewart, C., et al., *First proof of bismuth oxide nanoparticles as efficient radiosensitisers on highly radioresistant cancer cells.* Phys Med, 2016. **32**(11): p. 1444-1452.
37. Bogusz, K., et al., *Synthesis of potential theranostic system consisting of methotrexate-immobilized (3-aminopropyl)trimethoxysilane coated α-Bi2O3 nanoparticles for cancer treatment.* RSC Advances, 2014. **4**(46).
38. Shimizu, Y., et al., *H2 Sensing Properties of Metal Oxide Semiconductors as Varistor-Type Gas Sensors.* IEEJ Transactions on Sensors and Micromachines, 1997. **117**(11): p. 560-564.
39. Ambika, M.R., N. Nagaiah, and S.K. Suman, *Role of bismuth oxide as a reinforcer on gamma shielding ability of unsaturated polyester based polymer composites.* Journal of Applied Polymer Science, 2017. **134**(13).
40. Stewart, C., et al., *Engineering of Bismuth Oxide Nanoparticles to Induce Differential Biochemical Activity in Malignant and Nonmalignant Cells.* Particle & Particle Systems Characterization, 2014. **31**(9): p. 960-964.

41. Salazar-Pérez, A.J., et al., *Structural evolution of Bi2O3 prepared by thermal oxidation of bismuth nano-particles.* Sociedad Mexicana de Ciencia y Tecnología de Superficies y Materiales, 2005. **18**: p. 4 - 8.
42. Lopez-Salinas, F.I., et al., *Synthesis and characterization of nanostructured powders of Bi2O3, BiOCl and Bi.* Materials Letters, 2010. **64**(14): p. 1555-1558.
43. Kodama, H., A. Watanabe, and Y. Yajima, *Synthesis of a new bismuth oxide fluoride with the γ-Bi2O3 structure type.* Journal of Solid State Chemistry, 1987. **67**(1): p. 170-175.
44. Aidhy, D.S., et al., *Vacancy-Ordered Structure of Cubic Bismuth Oxide from Simulation and Crystallographic Analysis.* Journal of the American Ceramic Society, 2008. **91**(7): p. 2349-2356.
45. Cornei, N., et al., *New epsilon-Bi2O3 metastable polymorph.* Inorg Chem, 2006. **45**(13): p. 4886-8.
46. Gualtieri, A.F., S. Immovilli, and M. Prudenziati, *Powder X-ray diffraction data for the new polymorphic compound ω-Bi2O3.* Powder Diffraction, 2013. **12**(02): p. 90-92.
47. Qiu, Y., et al., *Controlled Synthesis of Bismuth Oxide Nanowires by an Oxidative Metal Vapor Transport Deposition Technique.* Advanced Materials, 2006. **18**(19): p. 2604-2608.
48. Anilkumar, M., R. Pasricha, and V. Ravi, *Synthesis of bismuth oxide nanoparticles by citrate gel method.* Ceramics International, 2005. **31**(6): p. 889-891.
49. Pan, C.Y., et al., *Synthesis of bismuth oxide nanoparticles by the polyacrylamide gel route.* Ceramics International, 2008. **34**(2): p. 439-441.
50. Jha, R.K., R. Pasricha, and V. Ravi, *Synthesis of bismuth oxide nanoparticles using bismuth nitrate and urea.* Ceramics International, 2005. **31**(3): p. 495-497.
51. Flores-Castaneda, M., et al., *Bismuth nanoparticles synthesized by laser ablation in lubricant oils for tribological tests.* Journal of Alloys and Compounds, 2015. **643**: p. S67-S70.
52. Rosa, R.G.T., et al., *Structural, morphological and optical properties of Bi NPs obtained by laser ablation and their selective detection of L-cysteine.* Colloids and Surfaces a-Physicochemical and Engineering Aspects, 2014. **457**: p. 368-373.
53. Verma, R.K., K. Kumar, and S.B. Rai, *Near infrared induced optical heating in laser ablated Bi quantum dots.* Journal of Colloid and Interface Science, 2013. **390**: p. 11-16.
54. Kusper, M. and G. Guisbiers, *Synthesis of aluminum oxide nanoparticles by laser ablation in liquids.* MRS Advances, 2018. **3**(64): p. 3899-3903.
55. Van Overschelde, O. and G. Guisbiers, *Photo-fragmentation of selenium powder by Excimer laser ablation in liquids.* Optics & Laser Technology, 2015. **73**: p. 156-161.
56. Gaikwad, S.H., S.V. Mahamuni, and M.A. Anuse, *Extractive spectrophotometric determination of bismuth(III) in alloy samples using 1-amino–4, 4, 6–trimethyl (1H, 4H) pyrimidine-2-thiol.* CSIR, 2005: p. 365-368.
57. Kopecka, B., V. Springer, and J. Turan, *Complexes of bismuth (HI) with ethylenediamine-2V,iV'-2,2'-di-(3-hydroxypropionic) acid.* Chemical Papers, 1975. **29**: p. 727.
58. Tauc, J., R. Grigorovici, and A. Vancu, *Optical Properties and Electronic Structure of Amorphous Germanium.* physica status solidi (b), 1966. **15**(2): p. 627-637.
59. Zhang, Q., et al., *From semiconductors to semimetals: bismuth as a photocatalyst for NO oxidation in air.* Journal of Materials Chemistry A, 2014. **2**(29): p. 11065-11072.
60. Ho, C.-H., et al., *The study of optical band edge property of bismuth oxide nanowires α-Bi2O3.* Optics Express, 2013. **21**: p. 11965-11972.
61. Balasubramanian, K., R. Udayabhaskar, and A. Kishore, *Optical and phonon properties of Sm-doped α-BiO micro rods.* Applied Physics A: Materials Science & Processing, 2014. **117**: p. 1409-1414.
62. Ho, C.H., et al., *The study of optical band edge property of bismuth oxide nanowires alpha-Bi2O3.* Opt Express, 2013. **21**(10): p. 11965-72.

63. Landa-Cánovas, Á.R., et al., *Transmission Electron Microscopy Study of Low Mo-content Bi-Mo-O Phases.* Microscopy and Microanalysis, 2012. **18**: p. 71-72.
64. Zhou, W., et al., *Superlattices in ternary oxides derived from bismuth oxide (Bi2O3): new families of ordered phases based on the fluorite structure.* Journal of Physical Chemistry, 1987. **91**: p. 512-514.
65. Doyle, P.A. and P.S. Turner, *Relativistic Hartree-Fock X-ray and electron scattering factors.* Acta Cryst. , 1968. **A24**: p. 390-397.
66. Campos, V., et al., *Bismuth and Silver Nanoparticles as Antimicrobial Agent over Subgingival Bacterial and Nosocomial Strains* Journal of Materials Science and Engineering A 2018. **8**: p. 142-146.
67. Luo, Y., et al., *Targeted nanoparticles for enhanced X-ray radiation killing of multidrug-resistant bacteria.* Nanoscale, 2013. **5**: p. 687-694.
68. Ai, K., et al., *Large-Scale Synthesis of Bi2S3 Nanodots as a Contrast Agent for In Vivo X-ray Computed Tomography Imaging.* Advanced Materials, 2011. **23**: p. 4886-4891.
69. Algethami, M., et al., *Radiation Dose Enhancement Using Bi2S3 Nanoparticles in Cultured Mouse PC3 Prostate and B16 Melanoma Cells.* NanoWorld Journal, 2015. **1**: p. 99-104.
70. Deng, J., et al., *Sequential delivery of bismuth nanoparticles and doxorubicin by injectable macroporous hydrogels for combined anticancer kilovoltage X-ray radio- and chemo-therapy.* Journal of Materials Chemistry B, 2018. **6**: p. 7966-7973.
71. Fu, P.P., et al., *Mechanisms of nanotoxicity: Generation of reactive oxygen species.* Journal of Food and Drug Analysis, 2014. **22**: p. 64-75.
72. Dayem, A.A., et al., *The Role of Reactive Oxygen Species (ROS) in the Biological Activities of Metallic Nanoparticles.* International Journal of Molecular Sciences, 2017. **18**: p. 120.
73. Ahamed, M., et al., *Oxidative stress mediated cytotoxicity and apoptosis response of bismuth oxide (Bi2O3) nanoparticles in human breast cancer (MCF-7) cells.* Chemosphere, 2019. **216**: p. 823-831.
74. Jiao, L., et al., *Nanocellulose Templated Growth of Ultra-Small Bismuth Nanoparticles for Enhanced Radiation Therapy.* Nanoscale, 2018. **10**: p. 6751-6757.
75. Ma, H., Z. Shen, and S. Ben, *Understanding the exfoliation and dispersion of MoS2 nanosheets in pure water.* Journal of Colloid and Interface Science, 2018. **517**: p. 204-212.
76. Guisbiers, G. and M. José-Yacaman, *Use of Chemical Functionalities to Control Stability of Nanoparticles.* Reference Module in Chemistry, Molecular Sciences and Chemical Engineering, 2018. **Encyclopedia of Interfacial Chemistry**: p. 875-885.
77. Tezel, F.M. and İ. Afşin Kariper, *Synthesis, surface tension, optical and dielectric properties of bismuth oxide thin film.* Materials Science-Poland, 2017. **35**(1): p. 87-93.
78. Guenther, G., R. Theissmann, and O. Guillon, *Size-Dependent Phase Transformations in Bismuth Oxide Nanoparticles. II. Melting and Stability Diagram.* The Journal of Physical Chemistry C, 2014. **118**(46): p. 27020-27027.
79. Fan, H.T., et al., *Optical properties of δ-Bi2O3 thin films grown by reactive sputtering.* Applied Physics Letters, 2005. **87**(23).
80. Slavin, Y.N., et al., *Metal nanoparticles: understanding the mechanisms behind antibacterial activity.* J Nanobiotechnology, 2017. **15**(1): p. 65.
81. Moreno-Álvarez, S.A., et al., *Preparation and bactericide activity of gallic acid stabilized gold nanoparticles.* Journal of Nanoparticle Research, 2010. **12**(8): p. 2741-2746.
82. Valodkar, M., et al., *Synthesis and anti-bacterial activity of Cu, Ag and Cu–Ag alloy nanoparticles: A green approach.* Materials Research Bulletin, 2011. **46**(3): p. 384-389.
83. Ahamed, M., et al., *Synthesis, Characterization, and Antimicrobial Activity of Copper Oxide Nanoparticles.* Journal of Nanomaterials, 2014. **2014**: p. 1-4.

84. Azam, A., et al., *Size-dependent antimicrobial properties of CuO nanoparticles against Gram-positive and -negative bacterial strains.* Int J Nanomedicine, 2012. **7**: p. 3527-35.
85. Thekkae Padil, V.V. and M. Cernik, *Green synthesis of copper oxide nanoparticles using gum karaya as a biotemplate and their antibacterial application.* Int J Nanomedicine, 2013. **8**: p. 889-98.
86. Siddique, S., et al., *Preparation, characterization and antibacterial activity of ZnO nanoparticles on broad spectrum of microorganisms.* Acta Chim Slov, 2013. **60**(3): p. 660-5.
87. Zarrindokht, E.-K., *Antibacterial activity of ZnO nanoparticle on Gram-positive and Gram-negative bacteria.* African Journal of Microbiology Research, 2012. **5**(18).
88. Zonaro, E., et al., *Biogenic selenium and tellurium nanoparticles synthesized by environmental microbial isolates efficaciously inhibit bacterial planktonic cultures and biofilms.* Front Microbiol, 2015. **6**: p. 584.